Chemical Science

ROYAL SOCIETY OF CHEMISTRY

EDGE ARTICLE

View Article Online
View Journal | View Issue

Cite this: *Chem. Sci.*, 2024, **15**, 1051

All publication charges for this article have been paid for by the Royal Society of Chemistry

Design of a bipolar organic small-molecule cathode with mesoporous nanospheres structure for long lifespan and high-rate Li-storage performance†

Simin Wang,‡[a] Qifei Guo,‡[b] Haoran Liu,[a] Longhai Zhang,[a] Chaofeng Zhang,[a] Tengfei Zhou,[a] Quanwei Ma,[a] Hongbao Li,*[a] Rui Wang[a] and Yang Zheng*[b]

Organic small-molecule compounds have become promising cathode materials for high-performance lithium-ion batteries (LIBs) due to their high theoretical capacity, efficient utilization of active sites, low cost, and sustainability. However, severe dissolution and poor electronic conductivity limit their further practical applications. Herein, we have synthesized an insoluble organic small molecule, ferrocenyl-3-(λ^1-azazyl) pyrazinyl [2,3-*f*] [1,10] phenanthrolino-2-amine (FCPD), by grafting ferrocene onto pyrazino [2,3-f] [1,10] phenanthroline-2,3-diamine (PPD). The combination of ferrocene (p-type Fe^{2+} moiety) and PPD (n-type C=N groups) in a bipolar manner endows the target FCPD cathode with an increased theoretical capacity and a wide voltage window. The highly conjugated π–π aromatic skeleton inside enhances FCPD's electron delocalization and promotes strong interaction between FCPD units. Additionally, the mesoporous structure within the FCPD can provide numerous electroactive sites, contact area, and ion diffusion channels. Benefiting from the bipolar feature, aromatic, and mesoporous structure, the FCPD cathode demonstrates a large capacity of 250 mA h g^{-1} at 0.1 A g^{-1}, a long lifespan of 1000 cycles and a high-rate capability of 151 mA h g^{-1} at 5 A g^{-1} along with a wide voltage window (1.2–3.8 V). Additionally, *in situ* synchrotron FT-IR and *ex situ* XPS reveal its dual ion storage mechanism in depth. Our findings provide essential insights into exploring the molecular design of advanced organic small molecules.

Received 1st November 2023
Accepted 6th December 2023

DOI: 10.1039/d3sc05843c

rsc.li/chemical-science

Introduction

Lithium-ion batteries (LIBs), as the most competitive batteries, provide power for a wide range of electronic products including portable devices, electric vehicles, and even grid energy storage systems.[1–6] Recently, various inorganic cathodes ($LiFePO_4$, $LiCoO_2$ and $LiMn_2O_4$) used in LIBs have been applied in practical applications and shown remarkable energy storage performance.[7–10] However, these traditional metal-based cathodes are primarily extracted from minerals or prepared at high temperature, which inevitably raises concerns about limited resources, significant energy consumption, and severe environmental pollution.[11–15] In contrast, organic compounds can be easily obtained from natural resources and possess characteristics such as resource sustainability, convenient synthesis, and the ability to easily adjust their molecular structure.[16–19] Moreover, organic electrodes undergo minimal structural changes and limited rearrangement, which makes them highly adaptable to ions of various sizes.[20–23] Consequently, organic electrode materials have emerged as promising alternatives to inorganic materials for next-generation batteries.[24–28]

Organic electrode materials can generally be classified into two categories based on different reaction mechanisms, n-type for cation storage and p-type for anion storage.[4,24] Among them, n-type organic cathodes have been extensively studied due to their high capacity. Examples of n-type organic cathodes include carbonyl compounds, imine-carbonyl compounds, imine compounds, and nitroaromatics. However, the low redox potential (<2.8 V *vs.* Li^+/Li) limits their practical applications. On the other hand, p-type organic cathodes offer a higher redox potential (>3 V *vs.* Li^+/Li), but their capacity is often limited. Examples of p-type organic cathodes are triphenylamine derivatives, triphenylphosphine derivatives, organosulfur compounds, and nitronyl nitroxide compounds. To address these limitations, a promising strategy is to combine both n-

[a]*Institutes of Physical Science and Information Technology, School of Materials Science and Engineering, Leibniz International Joint Research Center of Materials Sciences of Anhui Province, Anhui Province Key Laboratory of Environment-Friendly Polymer Materials, Key Laboratory of Structure and Functional Regulation of Hybrid Material (Ministry of Education), Anhui University, Hefei 230601, China. E-mail: lihb@ahu.edu.cn*

[b]*The State Key Laboratory of Refractories and Metallurgy, Institute of Advanced Materials and Nanotechnology, Wuhan University of Science and Technology, Wuhan 430081, China. E-mail: yzheng@wust.edu.cn*

† Electronic supplementary information (ESI) available. See DOI: https://doi.org/10.1039/d3sc05843c

‡ These authors contributed equally to this work.

type and p-type features in a bipolar manner, allowing for simultaneous cation and anion storage. This approach enables the achievement of an ideal potential and capacity. Bipolar organic cathodes, such as PANI, poly-quinone-phenylenediamine, and poly(1,8-diaminonaphthalene), have exhibited remarkable energy storage performance over the past few decades.[29] However, their large molecular weight and inactive units often result in low specific capacity. Additionally, the utilization of active sites within their polymer structures is typically inefficient.

In contrast, bipolar organic small-molecule compounds possess multiple redox groups, which can maximize the number of electrons transferred per unit and lead to highly efficient utilization.[30] However, issues with dissolution and low electronic conductivity limit their cycling stability and reaction kinetics. Polymerization and the integration of carbonaceous materials are considered powerful methods to address these issues, but significantly increased molecular weight and the inclusion of inactive composite will inevitably weaken their electrochemical performance.[31,32] By contrast, increasing the degree of π-conjugation should be considered as an effective method. This can effectively create and strengthen van der Waals interactions between neighboring organic small molecules, leading to a strong intermolecular π–π stacking. The strong π–π interaction can not only maintain the stable structure of small molecules during repeated lithiation/de-lithiation processes but also suppress their severe dissolution by forming aggregates or clusters.[33,34] Additionally, the greater delocalization of π electrons in these highly conjugated organic small molecules can enhance electronic conductivity.

In this study, we have designed and synthesized an organic small-molecule cathode by grafting ferrocene onto PPD, which we refer to as FCPD. FCPD possesses a bipolar feature and a high degree of π-conjugation simultaneously due to the p-type moiety (Fe^{2+}), n-type groups (C=N), and aromatic structure. The bipolar feature allows both the cation and anion to serve as charge carriers, resulting in a large capacity and a wide redox window. The high degree of π-conjugation facilitates charge transport and interaction between the small-molecule units, leading to fast kinetics and low solubility. As a result, the FCPD cathode exhibited excellent Li^+/anion-storage performance. Furthermore, density functional theory (DFT) calculations and *in/ex situ* spectra characteristics provide a detailed understanding of the Li^+/anion-storage mechanism of the FCPD cathode.

Experimental section

Synthesis of pyrazino[2,3-*f*] [1,10] phenanthroline-2,3-diamine (PPD)

PPD was synthesized *via* a three-step procedure, which refers to relevant literature.[35] Firstly, potassium phthalimide (14 mmol) was added to DMF solution, followed by vigorous stirring at 140 °C for 1 h under a nitrogen flow, and then 3,4-dichloro-1,2,5-thiadiazole (7 mmol) was slowly added to the solution and refluxed for 0.5 h. The residue was recrystallized with a mixture of trichloromethane and acetone (3 : 8 v/v). Secondly, the obtained light yellow needle crystal (1.26 mmol) and methylamine hydrochloride (1.5 g) were reflowed in a mixture of ammonia and DMF at 140 °C for 1 h, and then the solution was spun off. The obtained white solid and 1,10-phenanthroline-5,6-dione (0.8 mmol) were mixed in 30 mL ethanol at 70 °C for reflux for 4 h. Finally, the black solid was stirred in 75 mL ammonia solution to form a yellow solid. PPD was then obtained after drying at 60 °C in a vacuum overnight.

Synthesis of ferrocenyl-3-(λ^1-azazyl) pyrazinyl [2,3-*f*] [1,10] phenanthrolino-2-amine (FCPD)

21.4 mg (0.1 mmol) of FCA and 26.33 mg (0.1 mmol) of PPD were added into a Pyrex tube, and then 2 mL of *n*-BuOH with 0.5 mL of AcOH were added. Subsequently. The Pyrex tube was subsequently frozen and degassed under a liquid nitrogen bath at a temperature of 77 K. The freeze–pump–thaw cycle was repeated three times before the tube was sealed under vacuum. The sealed Pyrex tube was then sonicated to disperse monomers and kept at a temperature of 120 °C for a duration of 72 h. The crude product of FCPD precipitate was obtained through vacuum filtration. The product appeared reddish brown in color and was washed with DMF and acetone before being dried at 80 °C under vacuum.

Material characterization

Scanning electron microscopy (SEM, Regulus 8230) and transmission electron microscopy (TEM, JEM-2100) were applied to analyze the morphology of FCPD. Raman spectroscopy (LabRAM HR), Fourier transform infrared spectroscopy (FT-IR, Thermo Scientific Nicolet iS50), and X-ray photoelectron spectroscopy (XPS, Axis Ultra DLD Kratos Axis SUPRA) were used to test the physical properties of FCPD. N_2 adsorption–desorption isothermal analysis was performed using a Micromeritics APSP-2460 specific surface area analyzer. Thermogravimetric analysis (TGA) was conducted on an STA 449 F5 in the temperature range of 30 to 800 °C with a heating rate of 5 °C min^{-1} under air. The solubility of the samples in the electrolyte was determined by ultraviolet visible spectroscopy (UV-Vis, SPECORD 210).

Electrochemical measurements

The cathode is composed of 30 wt% FCPD, 60 wt% Ketjen black, and 10 wt% polyvinylidene difluorides. The above mixture was dispersed with *N*-methyl pyrrolidone to form a uniform slurry, and then coated onto Al–C foil. 2032-Type coin cells were assembled in a glove box with 1 M LiTFSI in DME/DOL as the electrolyte. The full oxidized state of FCPD and the reduced state of graphite were used as the cathode and anode, respectively, to assemble the full cells, which were tested from 1.0 to 3.0 V. The negative/positive ratio was about 1.34 : 1, and the dose of electrolyte (1 M LiTFSI in DME/DOL) is 50 μL. Charge/discharge tests and the galvanostatic intermittent titration technique (GITT) were carried out using a NEWARE (Shenzhen, China). The cyclic voltammetry curves (CV) and electrochemical impedance spectra (EIS) were recorded on a CHI 760E electrochemical workstation. The *in situ* synchrotron FT-IR data were collected *via* the infrared spectroscopy and microspectroscopy

beamline (BL01B). The FCPD cathode was assembled into a commercial *in situ* cell specially designed for FT-IR microspectroscopic measurement (Beijing Scistar Technology Co. Ltd). Afterward, a charge/discharge test was conducted at a rate of 0.05 A g^{-1} on the NEWARE battery tester.

Theoretical calculations

The structures of FCA, PPD, and FCPD were constructed and optimized at the B3LYP-D3(BJ)/6–311++G (b, p) level, which includes the dispersion interaction. The corresponding highest occupied molecular orbitals (HOMOs), the lowest unoccupied molecular orbitals (LUMOs), the density of states (DOS), and the electron density distribution were determined using the Multiwfn 3.8 program.[36] All the theoretical calculations were carried out using the Gaussian 16 software package.[37]

Results and discussion

The target FCPD compound was synthesized by grafting ferrocene onto PPD in *n*-BuOH solvent with AcOH as the catalyst. The synthesis was carried out at 120 °C for 72 h, as illustrated in Fig. 1a. To investigate the formation of FCPD and its detailed molecular structure, FT-IR spectra were firstly recorded and are presented in Fig. 1b. In comparison to the FCA and PPD monomers, the characteristic peak of aldehyde (–CHO) groups at 1675 cm^{-1} completely disappeared in the target FCPD compound. This disappearance was accompanied by an increase in the intensity of imide (C=N) groups at 1560 cm^{-1} and a decrease in the intensity of amino ($-NH_2$) groups at ≈3400 cm^{-1}.[38] This evolution demonstrates the consumption of –CHO/$-NH_2$ groups in FCA and PPD and the formation of the new C=N group in FCPD, confirming the successful combination between FCA and PPD.[39] It is important to note that the characteristic peak of the amino group is still detected in FCPD.

Furthermore, XPS analysis revealed the presence of C 1s, N 1s, and Fe 2p in FCPD (Fig. 1c–e). In the Fe 2p spectrum, the characteristic peaks at 708.1 and 720.8 eV correspond to Fe^{2+}, indicating the successful grafting of ferrocene.[38] The C 1s spectrum exhibits four peaks at 284.8, 285.7, 287.6, and 291.1 eV, which can be attributed to the C=C/C–C, C–N, and C=N bonds and the π–π satellite peak, respectively. The N 1s spectrum further shows the characteristic peaks of C–N (400.1 eV) and C=N (398.8 eV),[3,33,40,41] conforming the existence of these bonds in FCPD. Additionally, the N 1s spectrum contains

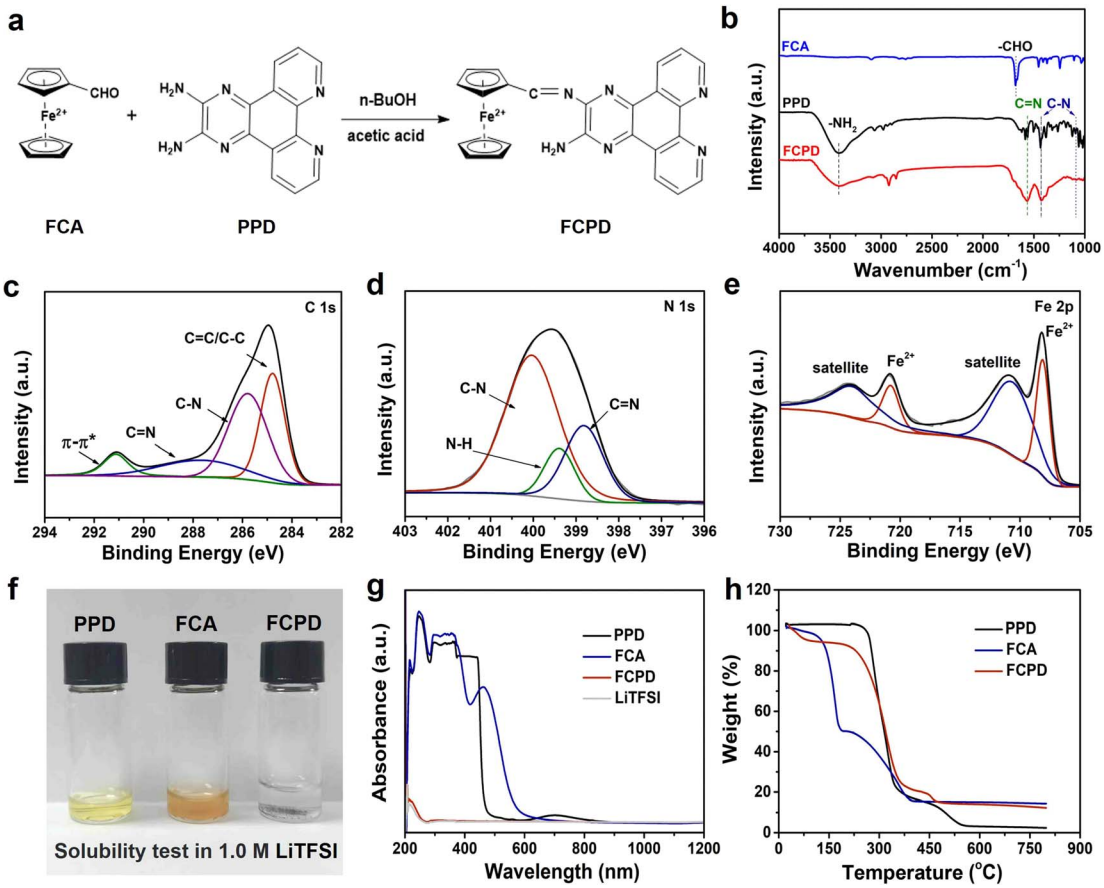

Fig. 1 (a) Schematic synthesis of the FCPD cathode. (b) FT-IR spectra of PPD, FCA, and FCPD. (c)–(e) High-resolution XPS spectra of C 1s, N 1s, and Fe 2p for FCPD. (f) Photographs of PPD, FCA, and FCPD soaked in an electrolyte (1 M LiTFSI in DME/DOL), respectively. (g) UV-vis spectra of the electrolyte (1 M LiTFSI in DME/DOL) and the electrolytes after soaking PPD, FCA, and FCPD. (h) Thermogravimetric analysis of PPD, FCA, and FCPD.

a peak at 399.3 eV related to the N–H bonds, which should be derived from the amino group in FCPD. Afterward, the solubility of the three small molecules (PPD, FCA, and FCPD) in the organic electrolyte was explored.

As shown in Fig. 1f, PPD and FCA-soaked electrolytes turn deep yellow and brown colors, respectively, indicating their high solubility. In contrast, the FCPD-soaked electrolyte is almost colorless, suggesting that the synthesized FCPD is much less soluble in the electrolyte. In addition, further UV-vis spectra of these soaked electrolytes are collected in Fig. 1g. It is evident that only the FCPD-soaked electrolyte exhibits a spectrum similar to that of the fresh electrolyte, providing further confirmation of its insolubility.[2,33] Furthermore, the TGA profiles of PPD, FCA, and FCPD are shown in Fig. 1h, revealing their respective thermal decomposition temperatures of 280, 130, and 260 °C. It should be note that both FCA and FCPD left residuals after annealing at 750 °C, which can be attributed to the oxidation of the ferrocene inside, further validating the successful ferrocene grafting.[38,42]

Afterwards, the microstructure of these organic materials was observed by SEM and TEM. Interestingly, unlike the irregular morphology of PPD and FCA monomers (Fig. S1a and b†), uniform nanospheres with a smooth surface were observed in FCPD, as displayed in Fig. 2a and b. Fig. 2c confirms the presence of these nanospheres with a diameter of approximately 720 nm, which is well consistent with further TEM image observations (Fig. 2d). Moreover, the corresponding energy-dispersive X-ray spectroscopy mapping images clearly illustrate the uniform distributions of C (purple), N (green), and Fe (red) species on the FCPD nanosphere (Fig. 2e). To examine the porosity of these FCPD nanospheres, N_2 adsorption–desorption isotherm was recorded at 77 K. As seen in Fig. 2f, FCPD exhibits a typical IV type feature, indicating the existence of mesopores within the FCPD nanospheres. The pore size distribution curve further confirms the size of mesopores, *i.e.*, ≈3.8 nm (the inset of Fig. 2f). The mesoporous structure in FCPD can significantly increase the contact area with the electrolyte and boost the ion diffusion, which can effectively increase the ion storage capacity and electrochemical kinetics.[43,44] Additionally, the Brunauer–Emmett–Teller (BET) surface area can be calculated to be 20.3 $m^2\ g^{-1}$.

To understand the molecular structure–property relationship, DFT calculations were performed. Fig. 3a displays the optimized molecule models (PPD, FCA, and FCPD) and corresponding molecular orbital energy levels (LUMO and HOMO). Among them, FCPD exhibits a lower LUMO value of −3.821 eV compared to that of PPD (−2.862 eV) and FCA (−3.508 eV). According to molecular orbital theory, a lower LUMO level corresponds to a higher electron affinity for the organic small molecule.[45] Meanwhile, the LUMO–HOMO energy gaps (ΔE) of PPD, FCA, and FCPD were calculated to be 2.086, 1.555, and 1.243 eV, respectively. The narrow gap in FCPD facilitates charge transfer, leading to higher electronic conductivity.[46] At the same time, an increase in the DOS for FCPD across the Fermi level (Fig. 3b) verifies the rapid charge transfer as well. In addition, according to the calculated molecular electrostatic potential (Fig. 3c), multiple regions around C=N groups show negative values. As is known, these regions are more conducive to capturing the cation (Li^+) and can be considered as the possible reactive sites. Therefore, according to the multiple active sites, FCPD will capture more Li ions per unit. In short, the aforementioned narrow gaps, increased DOS, and multiple active centers give the FCPD cathode enhanced electronic conductivity and storage capabilities.[19]

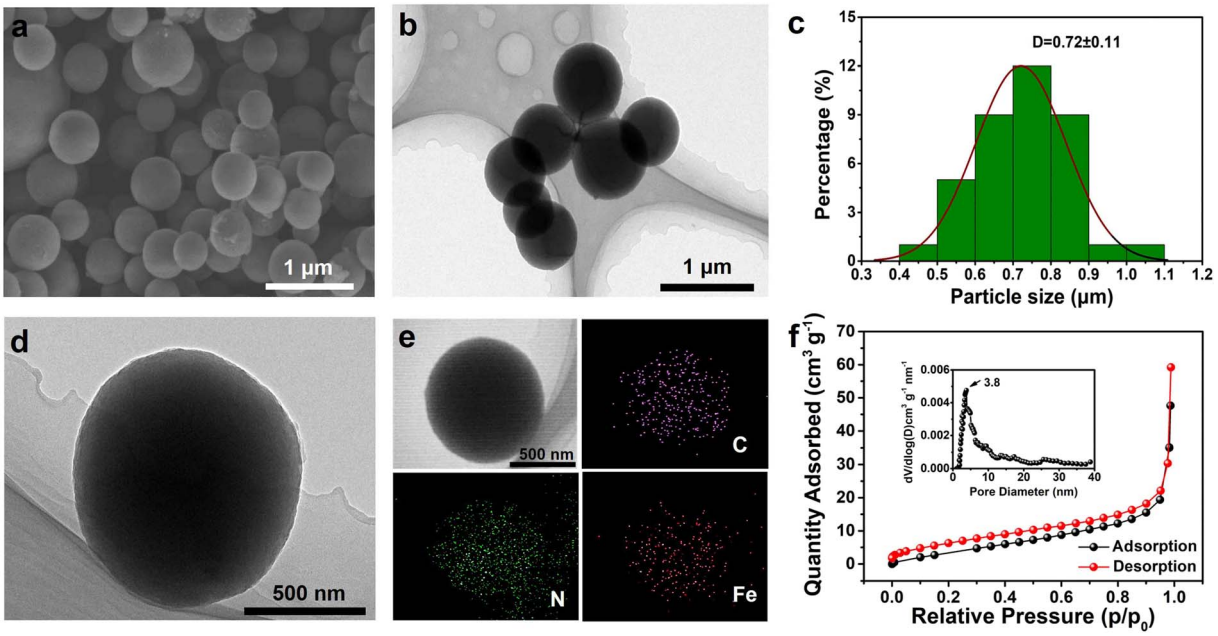

Fig. 2 (a) and (b) SEM and TEM images of the FCPD cathode and (c) corresponding histogram of size distribution. (d) and (e) TEM images of the FCPD cathode and corresponding elemental mapping images of C, N, and Fe. (f) N_2 adsorption–desorption isotherm of FCPD (inset shows the pore size distribution).

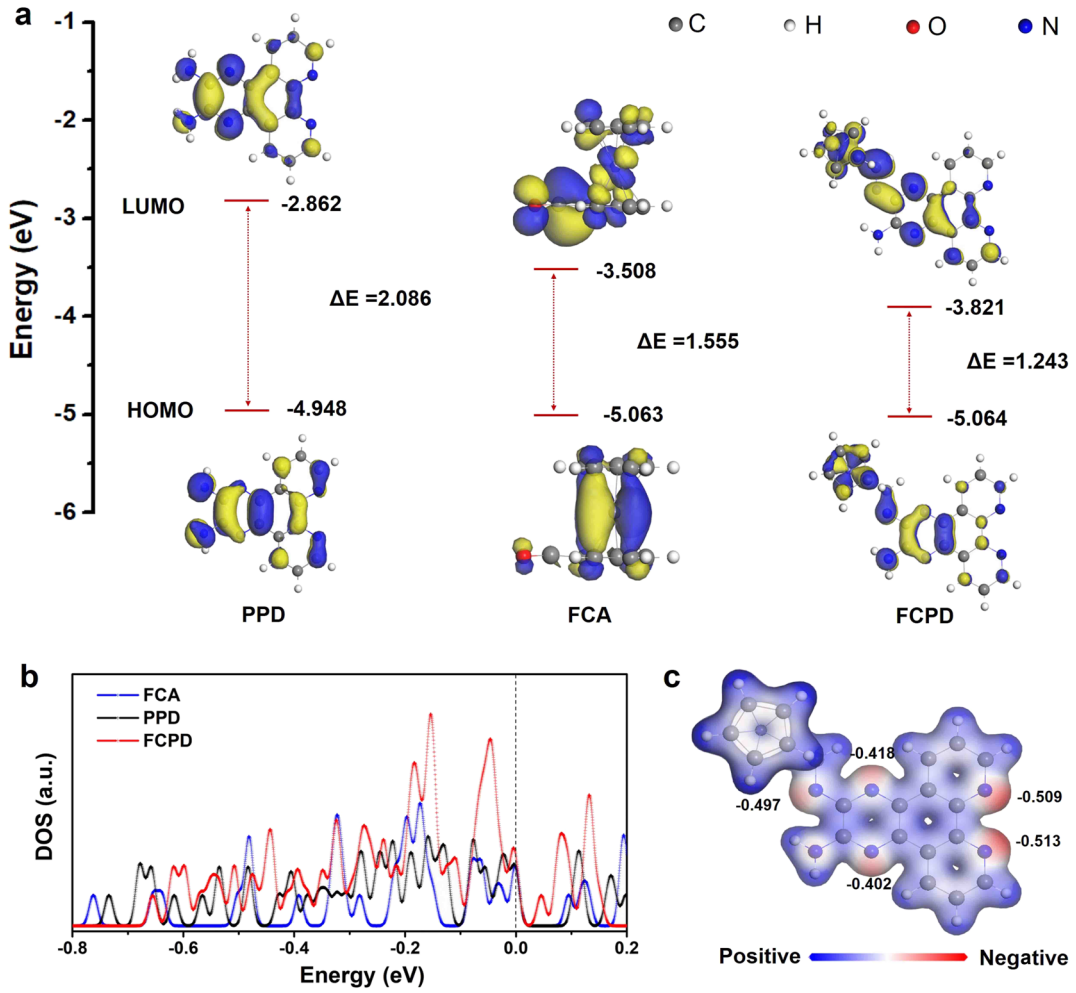

Fig. 3 (a) The calculated HOMO, LUMO, and (b) density of states for the FCA, PPD, and FCPD models. (c) Electron density distribution of the FCPD models.

To explore the electrochemical performance of the FCPD cathode, the CV curves of the initial three cycles were collected at a scan rate of 0.1 mV s^{-1} between 1.2 and 3.8 V (Fig. S2†). Obviously, two pair of redox peaks are observed, one in the low-potential (1.8 and 2.2 V) and the other in the high-potential region (2.3 and 3.2 V). The low-potential redox peaks are attributed to the n-type redox-active unit (C=N), while the high-potential redox peaks correspond to the p-type unit (Fe^{2+}). Such a typical bipolar feature helps expand its working potential window and theoretical capacity.

Subsequently, the rate capability of the samples was investigated at different current densities ranging from 0.1 to 5.0 A g^{-1}, as shown in Fig. 4a. The FCPD cathode exhibits high capacities of 250, 231, 213, 194, and 183 mA h g^{-1} at 0.1, 0.3, 0.5, 1.0, and 3.0 A g^{-1}, respectively. Even at the maximum current value of 5.0 A g^{-1}, it retains a reversible capacity of 151 mA h g^{-1}, which is competitive compared to reported values (Table S1†). Notably, even at various current densities, the corresponding charge/discharge profiles with FCPD still possess the bipolar feature (Fig. S3c†) as compared to PPD and FCA (Fig. S3a and b†), which is well consistent with the dQ/dV profiles (Fig. S3d–f†). FCPD exhibits clear platforms and characteristic peaks, indicative of n-type and p-type reactions, demonstrating remarkable stability and reversibility. When the current density returns to 0.1 A g^{-1}, a capacity of 240 mA h g^{-1} can be achieved, highlighting its good reversibility. In contrast, PPD and FCA cathodes exhibit fast capacity decay at different current densities, especially at 5.0 A g^{-1}, where only 75 mA h g^{-1} and 100 mA h g^{-1} are retained, which can be ascribed to their severe solubility in the electrolyte. Besides, the FCPD cathode shows attractive cycling performance at 0.1 A g^{-1}, as shown in Fig. 4b. Even after 100 cycles, it retains a discharge capacity as high as 249 mA h g^{-1}. The corresponding capacity fading rate is only 1.6% and it maintains an average coulombic efficiency of approximately 100% throughout the cycling. In contrast, PPD and FCA exhibit relatively low capacity and poor coulombic efficiency.

Fig. 4c shows a long-term cycling performance of the FCPD cathode at 5.0 A g^{-1}. Surprisingly, even after continuous 1000 cycles, the FCPD cathode still maintains a capacity as large as 150 mA h g^{-1}, corresponding to a high-capacity retention of 81.9%. This demonstrates its superior stability. To investigate

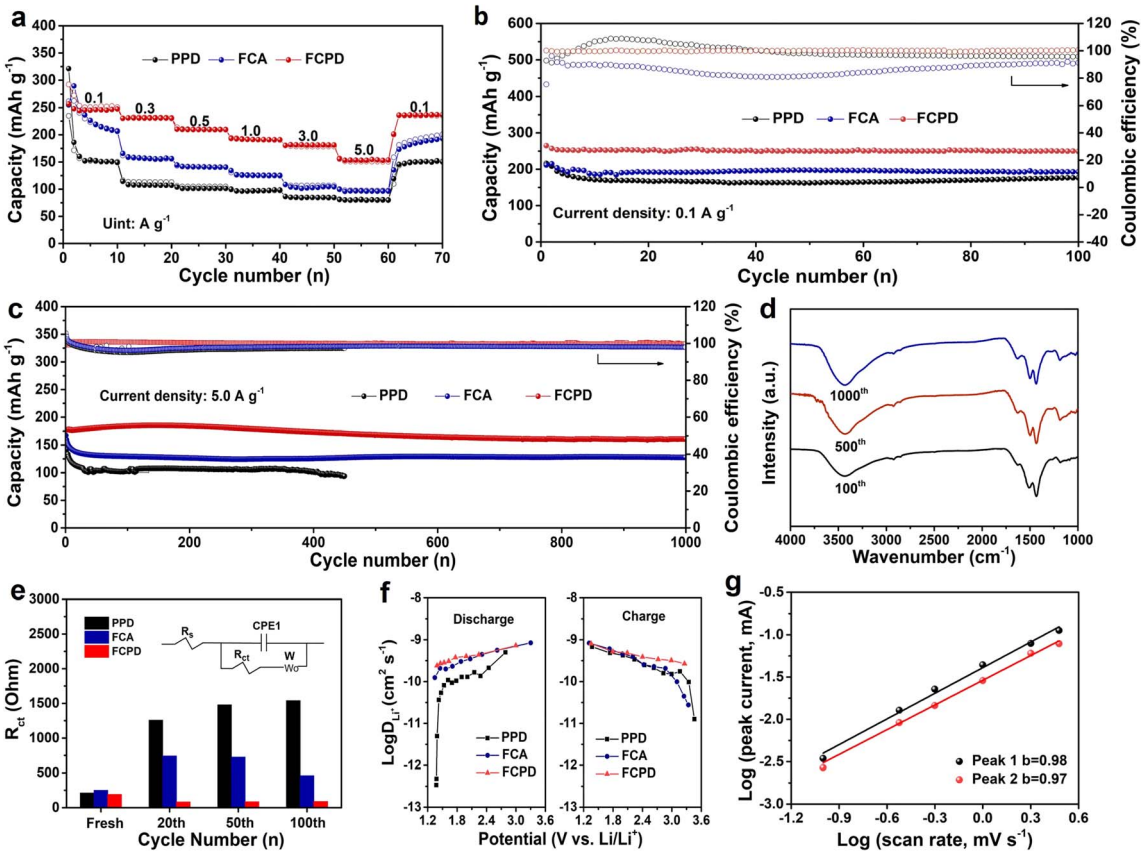

Fig. 4 (a) Rate capability, (b) cycling performance at 0.1 A g^{-1}, and (c) cycling performance at 5.0 A g^{-1} for the PPD, FCA, and FCPD cathodes. (d) FT-IR spectra of the FCPD cathode after different cycles at 5.0 A g^{-1}. (e) The calculated R_{ct} values of the PPD, FCA, and FCPD cathodes (the inset shows the equivalent circuit). (f) Li^+ diffusion coefficients of the PPD, FCA, and FCPD cathodes at different charge/discharge states. (g) The relationship between log(*i*) and log(*v*).

the remarkable cycling stability of FCPD, FT-IR spectroscopy was conducted for different numbers of cycles during its long-term cycling. As depicted in Fig. 4d, even after 100, 500, and 1000 cycles, no significant changes in the characteristic peaks of FCPD are observed in FT-IR spectra. This can be attributed to the cushioning effect of the mesoporous structure in FCPD. Afterward, EIS diagrams for PPD, FCA, and FCPD cathodes were collected to study their kinetics performance. As shown in Fig. S4,†[47,48] the semicircle in the high-middle frequency region represents the charge transfer resistance (R_{ct}). Coupled with the proposed equivalent circuit model (inset of Fig. 4e), the FCPD cathode exhibits the lowest R_{ct} (190.3 Ω) compared to those of PPD (212.1 Ω) and FCA (251.1 Ω) (Fig. 4e). More importantly, different from the large fluctuation of R_{ct} for PPD and FCA cathodes during the cycling (20th, 50th, and 100th cycles), the FCPD cathode just shows a slight change. This fast and stable charge transfer ensures that the FCPD cathode has ideal reaction kinetics during repeated lithiation/de-lithiation, which is closely related to its significant cycle and rate behavior.[49] Such excellent electrochemical performances can be attributed to its highly conjugated structure, which can significantly increase the intermolecular force, thus suppressing its high solubility in the electrolyte for high cycling stability (the capacity decay rate of FCPD is 18.1% after 1000 cycles at 5.0 A g^{-1}). By comparison, some organic cathode materials without the aromatic conjugated structure usually show rapid capacity decay. For example, the capacity decay rate of azine (N–N-linked diimine)-based polymers (P3)[50] is 15% after 200 cycles at 0.13 A g^{-1}; the capacity decay rate of benzo[*c*]thiophen-1(3*H*)-thione (DPTTO)[51] is 19% after 100 cycles at 0.05 A g^{-1}. Additionally, the resultant FCPD cathode exhibits extended conjugation, which ensures electron delocalization and a low energy gap, leading to high electronic conductivity.

To further reveal the electrochemical kinetics of the FCPD cathode, the Li^+ diffusion coefficients (D_{Li^+}) at different charge/discharge stages were calculated according to the GITT curves (Fig. S5†) and eqn (1).

$$D_{Li^+} = \left(\frac{4L^2}{\pi\tau}\right) \times \left(\frac{\Delta E_s}{\Delta E_t}\right)^2 \quad (1)$$

where L stands for the diffusion length of Li^+ and τ corresponds to the relaxation time. ΔE_s represents the change of stable potential after a single pulse. ΔE_t represents the change of potential during the pulse excluding the elimination of iR drop.[52] As seen in Fig. 4f, compared with PPD and FCA upon the charge/discharge processes, the D_{Li^+} of the FCPD cathode

exhibits higher and more stable evolutions, which are mainly concentrated around 10^{-10}–10^{-9} cm^2 s^{-1}. This phenomenon can be attributed to its spherical structure and mesoporous properties, which provide sufficient channels for ions to diffuse and the electrolyte to penetrate into FCPD.[53]

Subsequently, to understand the fast kinetics of the FCPD cathode, CV curves were collected under various scan rates ranging from 0.1 to 3.0 mV s^{-1}, as shown in Fig. S6.† The relationship between the scan rate (v) and peak current (i) can be described using eqn (2) and (3).

$$i = av^b \quad (2)$$

$$\log(i) = b\log(v) + \log(a) \quad (3)$$

where the b-value dominated the Li-storage behaviors, capacitive behavior (b = 1.0) or diffusion-controlled processes (b = 0.5). According to the linear correlation between log(i) and log(v), the b-values corresponding to the marked peaks 1 and 2 were calculated to be 0.98 and 0.97 (Fig. 4g), which are both close to 1.0, indicating the domination of a fast capacitive behavior in the FCPD cathode. In contrast, PPD and FCA exhibit relatively low b-values of 0.83/0.88 and 0.70/0.75 (between 0.5 and 1.0), respectively, suggesting the combination of diffusion and capacitive processes, as shown in Fig. S7.† Therefore, the FCPD cathode possesses faster electrochemical kinetics, which contribute to its excellent rate capability and cycling stability at high rates.

To reveal the storage mechanism of the FCPD cathode, *in situ* synchrotron FT-IR characterization was performed in different charge/discharge states. As shown in Fig. 5a–c, the 2nd charge/discharge profiles and corresponding *in situ* synchrotron FT-IR contour map were recorded. In the discharging process, the characteristic peaks related to the C=N bond (1550–1570 cm^{-1}) gradually decrease, accompanied by an increase of C–N bonds at around 1070 cm^{-1}.[54] This phenomenon can be ascribed to the Li reaction with C=N bonds, which leads to the consumption of C=N bonds and the formation of C–N–Li. Besides, the C–SO_2–N bond corresponding to the anions ($TFSI^-$) can be observed at around 1300 cm^{-1},[55] which presents the same evolution as for the C=N bond, indicating the participation of the anions ($TFSI^-$) in the reaction. Subsequently, a further charging process shows the recovery of these bonds, indicating their high reversibility as active sites in FCPD. In addition, the charge/discharge processes were further investigated by *ex situ* XPS measurement. As shown in Fig. 5d, a reversible change in peak intensity for Li 1s spectra is observed in the full charge and discharge states, indicating a reversible Li-storage behavior in FCPD. The N 1s spectrum (Fig. 5e) reveals two major peaks associated with the C=N and C–N bonds at 398.8 and 400.01 eV, respectively. The C=N bonds gradually decrease from the initial state to the full lithiation state, while the C–N bonds increase significantly, suggesting a transformation between C=N and C–N bonds.[56–58] After charging to 3.8 V, the peak of C=N bonds enhances obviously, accompanied by a decrease in the C–N bond

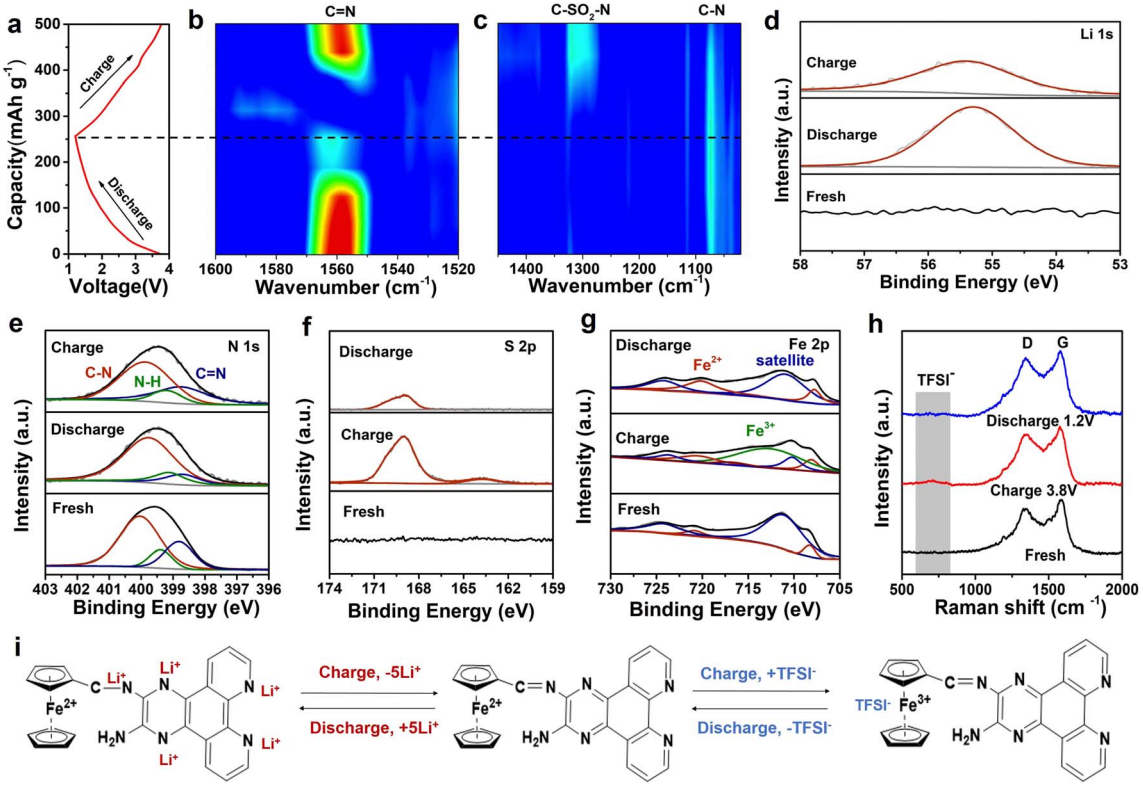

Fig. 5 (a) The 2nd charge/discharge profiles at 0.05 A g^{-1} and (b) and (c) corresponding *in situ* FT-IR contour map of the FCPD cathode. (d)–(g) High-resolution XPS spectra of Li 1s, N 1s, S 2p, and Fe 2p of the FCPD cathode at different charge/discharge states. (h) *Ex situ* Raman spectra of the FCPD cathode at different charge/discharge states. (i) Proposed dual ion storage mechanisms for the FCPD cathode.

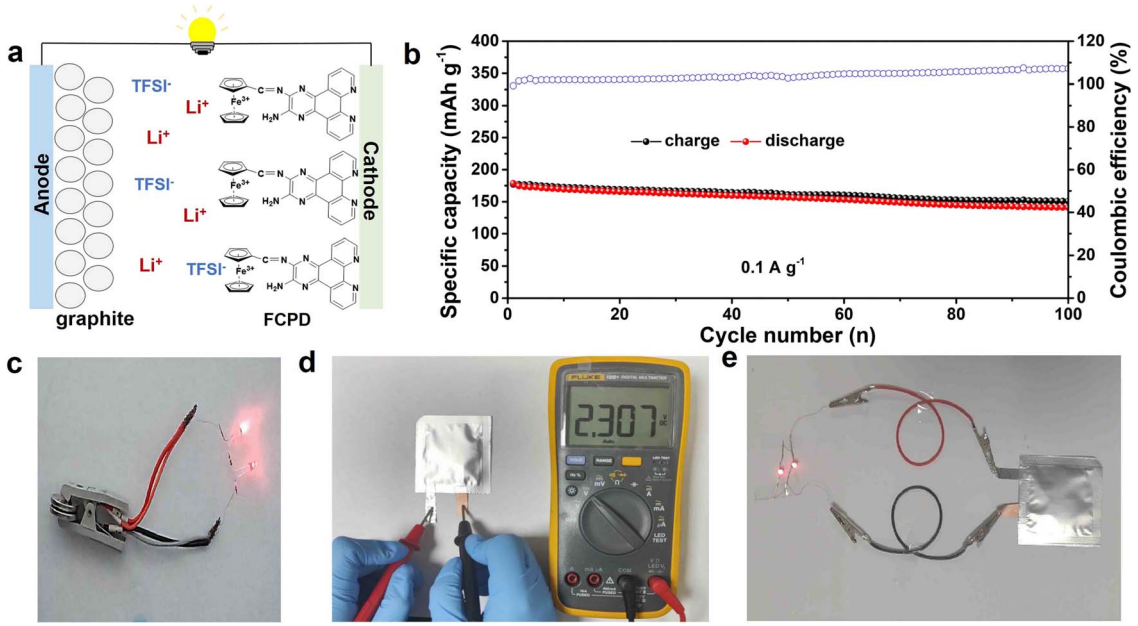

Fig. 6 (a) Schematic diagram of the graphite//FCPD full cell. (b) Cycling performance of the graphite//FCPD full cell at 0.1 A g^{-1}. (c) The digital photo of the full cell lighting diodes. (d) and (e) Practical evaluation of the graphite//FCPD pouch battery.

peak, demonstrating the revision of the C=N bonds from the C–N bonds. These findings further support the results obtained from *in situ* FT-IR spectra.

Notably, in addition to the reversible Li-storage in FCPD, the anions ($TFSI^-$) can also function as charge carriers for energy storage, just as shown in Fig. 5f. The S 2p spectrum exhibits the characteristic peak of $TFSI^-$, which appears in the charge state and disappears in the discharge state. Further *ex situ* Raman also shows the characteristic peak of $TFSI^-$ at 700–900 cm^{-1} and its reversible change, providing strong evidence for reversible anion storage in FCPD (Fig. 5h).[59] It is well known that, during the charge process, the p-type units are in a positively charged state and interact with the anions.[4] It is worth noting that during the charging, Fe^{2+} of the ferrocene could be oxidized to Fe^{3+}, resulting in a positively charged state. This state has been detected in the Fe 2p spectrum (Fig. 5g). Then, Fe^{3+} interacts with $TFSI^-$ to realize anion storage. Subsequently, Fe^{3+} would be reduced back to Fe^{2+} in the discharging process, leading to the recovery of the characteristic peaks of Fe^{2+}. In brief, the C=N bonds, severing as n-type active units in FCPD, reversibly participate in lithium storage, while Fe^{2+} acts as a p-type active unit for reversible $TFSI^-$ storage, just as illustrated in Fig. 5i. Finally, the potential application of FCPD was explored by using graphite as the anode to study the performance of graphite//FCPD full cells and pouch batteries (Fig. 6a and d). As depicted in Fig. 6b, the cell exhibits a high capacity of 145 mA h g^{-1} at 0.1 A g^{-1} after 100 cycles (based on cathode quality) and can light multiple diodes (Fig. 6c), indicating good cycling performance. In addition, as shown in Fig. 6d, the graphite//FCPD pouch cells can maintain a stable open-circuit voltage of 2.307 V, while being capable of illuminating two diodes continuously (Fig. 6e).

Conclusions

In summary, a bipolar organic small-molecule cathode called FCPD was successfully synthesized by grafting ferrocene onto PPD. The resulting FCPD cathode contains both n-type and p-type active sites, allowing dual ions (anions and cations) to act as charge carriers for energy storage. This design leads to a high theoretical capacity. Furthermore, the high electron delocalization and intermolecular interaction derived from the conjugated aromatic framework and abundant mesopores within FCPD can result in high electronic conductivity, fast ion diffusion, and limited solubility, which guarantee good reaction kinetics and stability. As a result, the FCPD cathode demonstrates impressive performance in LIBs. It exhibits a large capacity of 250 mA h g^{-1} at 0.1 A g^{-1}, a long lifespan of 1000 cycles and a high-rate capability of 151 mA h g^{-1} at 5 A g^{-1}. These excellent electrochemical properties highlight the great potential of conjugated bipolar small-molecule materials for energy storage applications.

Data availability

The data that support the findings of this study are openly available online.

Author contributions

H. B. L., Y. Z. and C. F. Z. designed and guided this experiment. S. M. W. and Q. F. G. carried out the experiment and materials characterization. H. R. L., L. H. Z., C. F. Z., T. F. Z., Q. W. M. and R. W. contributed to the data analysis and co-wrote the paper. H. B. L. and Y. Z. proposed and supervised the project.

Conflicts of interest

There are no conflicts to declare.

Acknowledgements

The authors acknowledge the financial support from the National Natural Science Foundation of China (52172173, 52302205, and 52002297), Natural Science Foundation of Anhui Province for Distinguished Young Scholars (2108085J25), Excellent Research and Innovation Team Project of Anhui Province (2022AH010001), Anhui Provincial Natural Science Foundation for Outstanding Young Scholar (2208085Y05), Anhui Provincial Scientific Reuter Foundation for Returned Scholars (2022LCX030), and Natural Science Foundation of Anhui Province (2208085QE130).

Notes and references

1 R. Wang, S. Xin, D. Chao, Z. Liu, J. Wan, P. Xiong, Q. Luo, K. Hua, J. Hao and C. Zhang, *Adv. Funct. Mater.*, 2022, **32**, 2207751.
2 W. Wang, Y. Tang, J. Liu, H. Li, R. Wang, L. Zhang, F. Liang, W. Bai, L. Zhang and C. Zhang, *Chem. Sci.*, 2023, **14**, 9033–9040.
3 Q. Ma, J. Zheng, H. Kang, L. Zhang, Q. Zhang, H. Li, R. Wang, T. Zhou, Q. Chen, A. Liu, H. Li and C. Zhang, *ACS Appl. Mater. Interfaces*, 2021, **13**, 43002–43010.
4 S. Lee, G. Kwon, K. Ku, K. Yoon, S.-K. Jung, H.-D. Lim and K. Kang, *Adv. Mater.*, 2018, **30**, 1704682.
5 D. Darbar, T. Malkowski, E. C. Self, I. Bhattacharya, M. V. V. Reddy and J. Nanda, *Mater. Today Energy*, 2022, **30**, 101173.
6 J. Zhou, Y. Liu, S. Zhang, T. Zhou and Z. Guo, *InfoMat*, 2020, **2**, 437–465.
7 Y. Lu, Q. Zhang, L. Li, Z. Niu and J. Chen, *Chem*, 2018, **4**, 2786–2813.
8 H. Wang, W. Zhang, J. Xu and Z. Guo, *Adv. Funct. Mater.*, 2018, **28**, 1707520.
9 B. Häupler, A. Wild and U. S. Schubert, *Adv. Energy Mater.*, 2015, **5**, 1402034.
10 Y. Liu, Z. Sun, X. Sun, Y. Lin, K. Tan, J. Sun, L. Liang, L. Hou and C. Yuan, *Angew. Chem., Int. Ed.*, 2020, **59**, 2473–2482.
11 D.-H. Yang, Z.-Q. Yao, D. Wu, Y.-H. Zhang, Z. Zhou and X.-H. Bu, *J. Mater. Chem. A*, 2016, **4**, 18621–18627.
12 Q. L. Jiang, K. Du, Y. B. Cao, Z. D. Peng, G. R. Hu and Y. X. Liu, *Chin. Chem. Lett.*, 2010, **21**, 1382–1386.
13 Z. Dong Peng, Y. Bing Cao, G. Rong Hu, K. Du, X. Guang Gao and Z. Wei Xiao, *Chin. Chem. Lett.*, 2009, **20**, 1000–1004.
14 J. Zhou, S. Zhang, Y.-N. Zhou, W. Tang, J. Yang, C. Peng and Z. Guo, *Electrochem. Energy Rev.*, 2021, **4**, 219–248.
15 W. Wang, S. Wang, L. Zhang, S. Hu, X. Xiong, T. Zhou and C. Zhang, *Research and Application of Materials Science*, 2022, **4**, 31–41.
16 T. Shi, G. Li, Y. Han, Y. Gao, F. Wang, Z. Hu, T. Cai, J. Chu and Z. Song, *Energy Storage Mater.*, 2022, **50**, 265–273.
17 H. Kang, Q. Chen, Q. Ma, L. Zhang, Q. Yang, H. Li, X. Xie, S. Lan and C. Zhang, *J. Power Sources*, 2022, **545**, 231951.
18 P. Xiong, S. Zhang, R. Wang, L. Zhang, Q. Ma, X. Ren, Y. Gao, Z. Wang, Z. Guo and C. Zhang, *Energy Environ. Sci.*, 2023, **16**, 3181–3213.
19 L. Zhang, R. Wang, Z. Liu, J. Wan, S. Zhang, S. Wang, K. Hua, X. Liu, X. Zhou, X. Luo, X. Zhang, M. Cao, H. Kang, C. Zhang and Z. Guo, *Adv. Mater.*, 2023, **35**, 2210082.
20 T. Sun and H. J. Fan, *Curr. Opin. Electrochem.*, 2021, **30**, 100799.
21 K. Zhu, C. Guo, W. Gong, Q. Xiao, Y. Yao, K. Davey, Q. Wang, J. Mao, P. Xue and Z. Guo, *Energy Environ. Sci.*, 2023, **16**, 3612–3622.
22 G. Li, Z. Zhao, S. Zhang, L. Sun, M. Li, J. A. Yuwono, J. Mao, J. Hao, J. Vongsvivut, L. Xing, C.-X. Zhao and Z. Guo, *Nat. Commun.*, 2023, **14**, 6526.
23 Y. Lyu, J. A. Yuwono, P. Wang, Y. Wang, F. Yang, S. Liu, S. Zhang, B. Wang, K. Davey, J. Mao and Z. Guo, *Angew. Chem., Int. Ed.*, 2023, **62**, 1–9.
24 Y. Lu and J. Chen, *Nat. Rev. Chem*, 2020, **4**, 127–142.
25 Z. Sun, Y. Liu, W. Ye, J. Zhang, Y. Wang, Y. Lin, L. Hou, M.-S. Wang and C. Yuan, *Angew. Chem., Int. Ed.*, 2021, **60**, 7180–7187.
26 Y. Zhe, Z. Chaoliang, W. Zhicheng, Z. Jianjian, L. Huirong, F. Jiameng, L. Jianling and K. Feiyu, *Energy Mater.*, 2022, **2**, 200006.
27 B.-W. Zhang, L. Cao, C. Tang, C. Tan, N. Cheng, W.-H. Lai, Y.-X. Wang, Z.-X. Cheng, J. Dong, Y. Kong, S.-X. Dou and S. Zhao, *Adv. Mater.*, 2023, **35**, 2206828.
28 H. Yang, Y. Lei, Q. Yang, B.-W. Zhang, Q. Gu, Y.-X. Wang, S. Chou, H.-K. Liu and S.-X. Dou, *Electrochim. Acta*, 2023, **439**, 141652.
29 Z. Li, J. Tan, Y. Wang, C. Gao, Y. Wang, M. Ye and J. Shen, *Energy Environ. Sci.*, 2023, **16**, 2398–2431.
30 N. Wang, Z. Guo, Z. Ni, J. Xu, X. Qiu, J. Ma, P. Wei and Y. Wang, *Angew. Chem., Int. Ed.*, 2021, **60**, 20826–20832.
31 Z. Wu, J. Xie, Z. J. Xu, S. Zhang and Q. Zhang, *J. Mater. Chem. A*, 2019, **7**, 4259–4290.
32 Z. Liu, R. Wang, Q. Ma, H. Kang, L. Zhang, T. Zhou and C. Zhang, *Carbon Neutralization*, 2022, **1**, 126–139.
33 H. Li, J. Wu, H. Li, Y. Xu, J. Zheng, Q. Shi, H. Kang, S. Zhao, L. Zhang, R. Wang, S. Xin, T. Zhou and C. Zhang, *Chem. Eng. J.*, 2022, **430**, 132704.
34 X. Ye, X. Rui, X. Lei, D. Jun-Fan and H. Jia-Qi, *Energy Mater.*, 2021, **1**, 100013.
35 M.-F. Wang, R. Yang, S.-J. Tang, Y.-A. Deng, G.-K. Li, D. Zhang, D. Chen, X. Ren and F. Gao, *Angew. Chem., Int. Ed.*, 2022, **61**, 1–9.
36 T. Lu and F. Chen, *J. Comput. Chem.*, 2012, **33**, 580–592.
37 M. J. Frisch, G. E. Scuseria, M. A. Robb, J. R. Cheeseman, G. Scalmani, V. Barone, B. Mennucci, G. A. Petersson, H. Nakatsuji, M. Caricato, X. Li, H. P. Hratchian, A. F. Izmaylov, J. Bloino, G. Zheng, J. L. Sonnenberg, M. Hada, M. Ehara, K. Toyota, R. Fukuda, J. Hasegawa, M. Ishida, T. Nakajima, Y. Honda, O. Kitao, H. Nakai, T. Vreven, J. A. Jr, J. E. Peralta, F. Ogliaro, M. Bearpark, J. J. Heyd, E. Brothers, K. N. Kudin, V. N. Staroverov,

R. Kobayashi, J. Normand, K. Raghavachari, A. Rendell, J. C. Burant, S. S. Iyengar, J. Tomasi, M. Cossi, N. Rega, J. M. Millam, M. Klene, J. E. Knox, J. B. Cross, V. Bakken, C. Adamo, J. Jaramillo, R. Gomperts, R. E. Stratmann, O. Yazyev, A. J. Austin, R. Cammi, C. Pomelli, J. W. Ochterski, R. L. Martin, K. Morokuma, V. G. Zakrzewski, G. A. Voth, P. Salvador, J. J. Dannenberg, S. Dapprich, A. D. Daniels, O. Farkas, J. B. Foresman, J. V. Ortiz, J. Cioslowski and D. J. Fox, *Gaussian 16 revision A.03*, Gaussian, Inc., Wallingford CT, 2016.

38 Y. Zhao, N. Xu, M. Ni, Z. Wang, J. Zhu, J. Liu, R. Zhao, H. Zhang, Y. Ma, C. Li and Y. Chen, *Adv. Mater.*, 2023, **35**, 2211152.

39 M. Wu, Y. Zhao, R. Zhao, J. Zhu, J. Liu, Y. Zhang, C. Li, Y. Ma, H. Zhang and Y. Chen, *Adv. Funct. Mater.*, 2022, **32**, 2107703.

40 H. Li, W. Zhang, J. Xu, L. Cai, Z. Yu, T. Ma, Y. Zheng, L. Wang and G. Yu, *Adv. Mater. Interfaces*, 2021, **8**, 2100943.

41 Y. Chen, J. Li, Q. Zhu, K. Fan, Y. Cao, G. Zhang, C. Zhang, Y. Gao, J. Zou, T. Zhai and C. Wang, *Angew. Chem., Int. Ed.*, 2022, **61**, 1–9.

42 C. Li, C. Zhang, J. Xie, K. Wang, J. Li and Q. Zhang, *Chem. Eng. J.*, 2021, **404**, 126463.

43 Z. Chen, S. Mei, W. Li, N. Xu, Y. Dong, Y. Jin, M. Ouyang and C. Zhang, *J. Mater. Chem. A*, 2021, **9**, 27010–27018.

44 F.-Z. Zhang, Y.-Y. Ma, M.-M. Jiang, W. Luo and J.-P. Yang, *Rare Metals*, 2022, **41**, 1276–1283.

45 Z. Ye, S. Xie, Z. Cao, L. Wang, D. Xu, H. Zhang, J. Matz, P. Dong, H. Fang, J. Shen and M. Ye, *Energy Storage Mater.*, 2021, **37**, 378–386.

46 Q. Chen, H. Li, H. Li, R. Wang, Q. Ma, L. Zhang and C. Zhang, *Chin. Chem. Lett.*, 2023, **34**, 107402.

47 J. Hao, L. Yuan, Y. Zhu, M. Jaroniec and S.-Z. Qiao, *Adv. Mater.*, 2022, **34**, 2206963.

48 S. Cruz-Manzo, P. Greenwood and R. Chen, *J. Electrochem. Soc.*, 2017, **164**, A1446.

49 Y. Zhai, H. Li, Q. Ma, R. Wang, L. Zhang and C. Zhang, *Ionics*, 2023, **29**, 1301–1310.

50 P. Acker, M. E. Speer, J. S. Wössner and B. Esser, *J. Mater. Chem. A*, 2020, **8**, 11195–11201.

51 B. Zhang, X. Yang, B. He, Q. Wang, Z. Liu, D. Yu and G. He, *J. Mater. Chem. A*, 2021, **9**, 14444–14450.

52 S. Zhang, L. Qiu, Y. Zheng, Q. Shi, T. Zhou, V. Sencadas, Y. Xu, S. Zhang, L. Zhang, C. Zhang, C.-L. Zhang, S.-H. Yu and Z. Guo, *Adv. Funct. Mater.*, 2021, **31**, 2006425.

53 G. Zhu, R. Guo, W. Luo, H. K. Liu, W. Jiang, S. X. Dou and J. Yang, *Natl. Sci. Rev.*, 2020, **8**, nwaa152.

54 T. Sun, W. Zhang, Z. Zha, M. Cheng, D. Li and Z. Tao, *Energy Storage Mater.*, 2023, **59**, 102778.

55 X. He, J. M. Larson, H. A. Bechtel and R. Kostecki, *Nat. Commun.*, 2022, **13**, 1398.

56 M.-S. Wu, N. T. H. Luu, T.-H. Chen, H. Lyu, T.-W. Huang, S. Dai, X.-G. Sun, A. S. Ivanov, J.-C. Lee, I. Popovs and W. Kaveevivitchai, *Adv. Energy Mater.*, 2021, **11**, 2100330.

57 W. Wang, V. S. Kale, Z. Cao, S. Kandambeth, W. Zhang, J. Ming, P. T. Parvatkar, E. Abou-Hamad, O. Shekhah, L. Cavallo, M. Eddaoudi and H. N. Alshareef, *ACS Energy Lett.*, 2020, **5**, 2256–2264.

58 M. Mao, C. Luo, T. P. Pollard, S. Hou, T. Gao, X. Fan, C. Cui, J. Yue, Y. Tong, G. Yang, T. Deng, M. Zhang, J. Ma, L. Suo, O. Borodin and C. Wang, *Angew. Chem., Int. Ed.*, 2019, **58**, 17820–17826.

59 Z. Wang, X. Li, W. Guo and Y. Fu, *Adv. Funct. Mater.*, 2021, **31**, 2009875.